Volume 5
Number 14
21 July 2024
Pages 5675–6018

Materials Advances

rsc.li/materials-advances

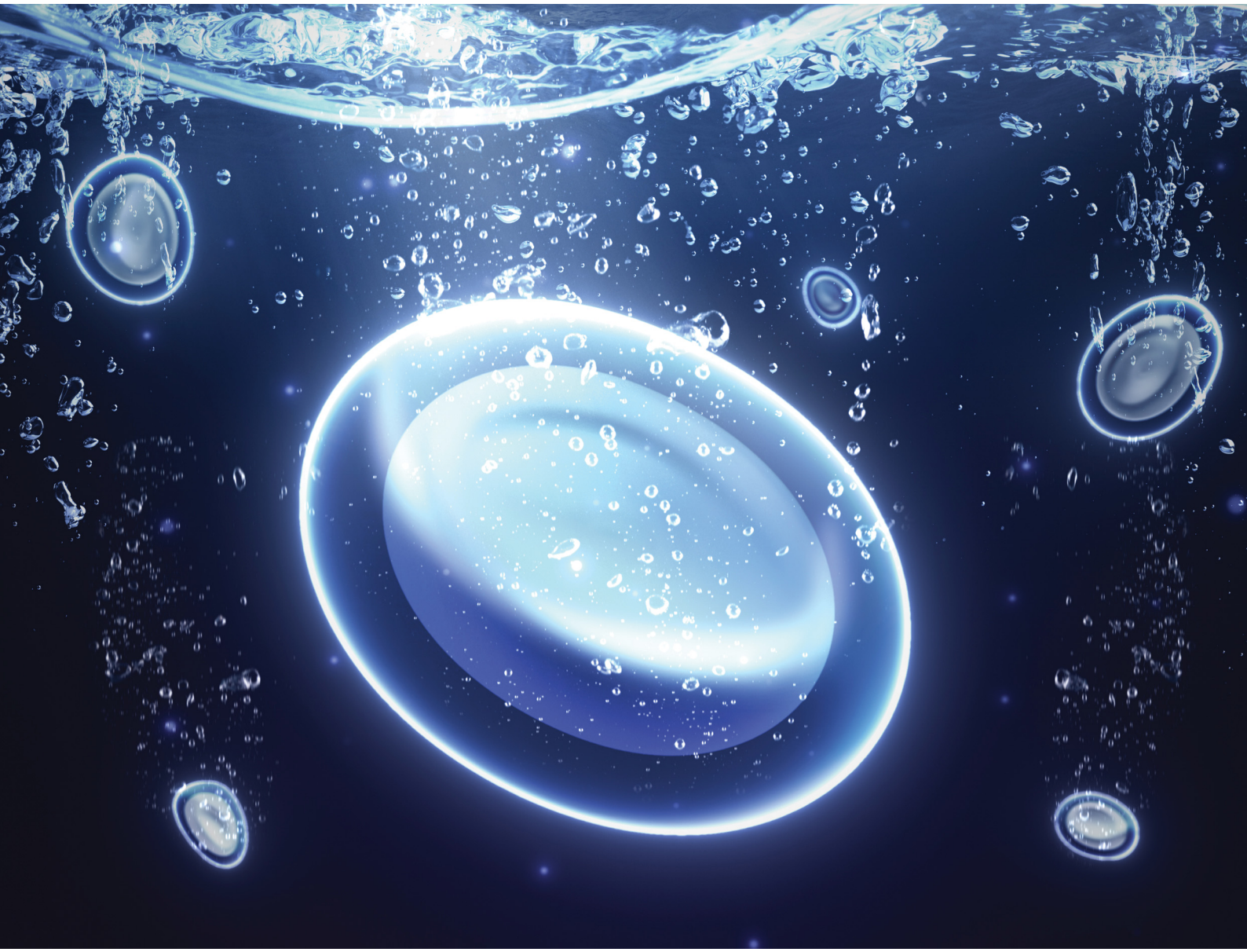

ISSN 2633-5409

ROYAL SOCIETY OF CHEMISTRY

PAPER

Zhang Qiming, Taichi Ito *et al.*

Development of rapid hypoxia-detectable artificial oxygen carriers with a core–shell structure and erythrocyte mimetic shape

Materials Advances

ROYAL SOCIETY OF CHEMISTRY

PAPER

View Article Online
View Journal | View Issue

Cite this: *Mater. Adv.*, 2024, 5, 5687

Development of rapid hypoxia-detectable artificial oxygen carriers with a core–shell structure and erythrocyte mimetic shape†

Zhang Qiming, *[a] Natsuko F. Inagaki, [a] Yusuke Hirabayashi,[b] Masamichi Kamihira[c] and Taichi Ito *[de]

Human red blood cells (RBCs) play a crucial role in delivering oxygen to tissues, and this function is closely linked to the fate of these cells, including their growth, differentiation, and survival. Inspired by RBCs, we propose a concave-shaped deformable perfluorocarbon-based oxygen carrier (cDFC) with a hypoxia-detectable function, based on a novel (PDMS) thermoplastic elastomer (PDMS-TPE), called a bifunctional cDFC, with a morphology similar to that of human RBCs. We prepared (PFOB)/PDMS-TPE cDFCs *via* Shirasu porous glass membrane emulsification (SPG ME), while adding tris(4,7-diphenyl-1,10-phenanthroline)ruthenium(II) (Ru(dpp)), platinum(II) octaethylporphine (PtOEP), and platinum(II) octaethylporphine (PtTFPP) to the dispersed phase to be immobilized in the PDMS-TPE shell as oxygen sensors. Among the three oxygen probes, PtOEP-loaded PFOB/PDMS-TPE exhibited the highest sensitivity to the dissolved oxygen concentration, with a K_{sv} value of 14. The bifunctional cDFCs also exhibited high biocompatibility *in vitro*, high stability, and negligible leaching of probe molecules in cell culture. Bifunctional cDFCs have potential for precise oxygenation in biomedical applications. Moreover, the illuminance response of cDFCs to a sudden drop of dissolved oxygen was fast, which was supported by numerical predictions using a diffusion equation model. The bifunctional cDFCs showed both rapid oxygen release and absorption and prompt detection of the oxygen concentration based on experiments and mathematical modeling.

Received 17th December 2023,
Accepted 22nd March 2024

DOI: 10.1039/d3ma01135f

rsc.li/materials-advances

Introduction

Oxygen is essential for human survival. Consequently, human red blood cells (RBCs) serve as ''oxygen carriers,'' encapsulating hemoglobin as they flow through the bloodstream within blood vessels.[1] The local oxygen concentration, or the partial pressure of oxygen in tissues or blood, reflects the fate of local cells, including their growth, differentiation, and death.[2] Increased cellular oxygen levels are associated with tissue damage, inflammation, and cancer.[3] Thus, the degree of hemoglobin desaturation (decrease in oxygen content) is intimately tied to tissue oxygen demand.[4] To manage a patient's blood oxygen concentration in the clinic, the absorbance differences between oxyhemoglobin (HbO_2) and deoxyhemoglobin (Hb) in both red light (at 660 nm) and near-infrared light (NIR) (at 940 nm) in the blood are utilized for an oxygen pulse meter, which can monitor the patient's blood oxygen content in real time.[5,6] Thus, RBCs function as both oxygen carriers and sensors.

In tissue engineering, artificial oxygen carriers (AOCs), which are alternatives to red blood cells, have been studied to achieve sufficient oxygen supply in a perfusion culture system for the oxygenation of regenerated tissues. However, precise control of the oxygen supply remains a challenge and is urgently required in various tissue engineering fields, such as the heart.[7,8] Perfluorocarbon (PFC)-based oxygen carriers (PFOCs) are a major type of AOC that feature high oxygen capacity and chemical inertness owing to the highly nonpolar chemical structure of PFC. Recently, micro-sized PFOCs have attracted attention owing to their core–shell structure, which favors the sustainable release of oxygen and long-term circulation. With the encapsulation of PFC into polymeric or lipid shells, these oxygen carriers exhibit excellent deformability and biocompatibility.[9–12]

[a] *Department of Chemical System Engineering, School of Engineering, The University of Tokyo, 7-3-1 Hongo, Bunkyo-ku, Tokyo 113-8656, Japan*
[b] *Department of Chemistry and Biotechnology, School of Engineering, The University of Tokyo, 7-3-1 Hongo, Bunkyo-ku, Tokyo 113-8656, Japan*
[c] *Department of Chemical Engineering, Kyushu University, 744 Motooka, Nishi-ku, Fukuoka 819-0395, Japan*
[d] *Department of Bioengineering, School of Engineering, The University of Tokyo, 7-3-1 Hongo, Bunkyo-ku, Tokyo 113-8656, Japan. E-mail: itotaichi@g.ecc.u-tokyo.ac.jp*
[e] *Department of Radiology and Biomedical Engineering, School of Medicine, The University of Tokyo, 7-3-1 Hongo, Bunkyo-ku, Tokyo 113-0033, Japan*

† Electronic supplementary information (ESI) available. See DOI: https://doi.org/10.1039/d3ma01135f

We previously developed monodispersed PFC microdroplets[13] and Hb microcapsules[14] as oxygen carriers using the Shirasu porous glass membrane emulsification (SPG ME) technique, which is an effective approach for preparing monodispersed core–shell microdroplets.[15] We then developed concave-shaped deformable perfluorocarbon-based oxygen carriers (cDFCs) that mimic RBC morphology and size using a thermoplastic elastomer (TPE) PLC as the shell.[9]

Subsequently, we developed new cDFCs using thermoplastic PDMS, which does not require curing for chemical crosslinking.[16] This resulted in new cDFCs and PFOB/PDMS TPE core–shell AOCs, which exhibited higher deformability and a spontaneous concave shape.[17] However, although precise oxygen concentration management is important, to the best of our knowledge, oxygen concentration-detectable micro-sized PFOCs have not yet been reported. Inspired by the multiple functions of RBCs, we designed new cDFCs with sustainable oxygen supplementation and real-time oxygen concentration analyses.

Because the phosphorescence or photoexcited state of some metal complex molecules is reversibly quenched by oxygen, they can dynamically and ratiometrically reflect the dissolved oxygen (DO) value of their circumstance.[18–20] As potential oxygen molecular probes polypyridyl complexes, such as tris(4,7-diphenyl-1,10-phenanthroline)ruthenium(II) dichloride (Ru(dpp)), and metalloporphyrin indicator molecules, such as platinum(II) octaethylporphine (PtOEP) and platinum(II) octaethylporphyrin (PtTFPP), are commonly used as DO indicators for biosensing.[18] Ruthenium complexes were first applied as oxygen indicators in the early 1960s, whereas platinum complexes were investigated later and have become popular in recent years because of their higher sensitivity, quicker response, larger Stokes shift, and higher photochemical stability.[21,22] They have been adopted in various biomedical devices[23] for clinical noninvasive real-time monitoring,[24,25] imaging of oxygen distribution in live cells and tissues,[26,27] and ratiometric sensing of oxygen levels in biological systems.[28–30] These oxygen probes are typically immobilized on a polymeric matrix because of their poor solubility and dispersibility in aqueous media. Among the matrix polymers, PDMS has been widely used as a substrate for oxygen probes owing to its high transparency and stability.[31]

In this study, Ru(dpp), PtOEP, and PtTFPP were first loaded onto cDFC and perfluorooctyl bromide (PFOB)/PDMS TPE core–shell AOCs to achieve RBC-like bifunctions for oxygen delivery and detection, as shown in Fig. 1. SPG ME, followed by evaporation-induced phase separation (EIPS), was used to prepare the oxygen-probe-loaded cDFCs (Fig. 1(B)). The three cDFCs were evaluated and compared using confocal laser scanning microscopy, scanning electron microscopy, two-dimensional cell culture, and microchannel chips to determine the optimal bifunctional oxygen carriers in terms of morphology, oxygen sensitivity, stability, and biocompatibility, using a confocal laser scanning microscope (CLSM), scanning electron microscope, two-dimensional (2D) cell culture, and microchannel chips. Finally, oxygen release kinetics were numerically simulated based on the mass transport equation model using

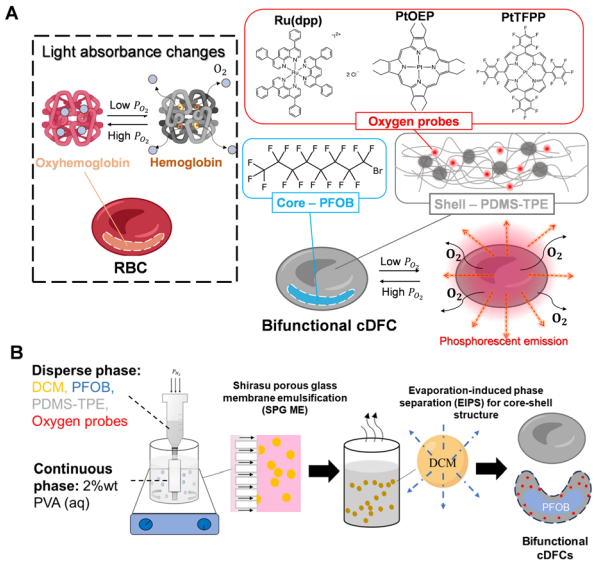

Fig. 1 Concept and fabrication process of hypoxia-detectable concave deformable perfluorocarbon-based oxygen carriers (called bifunctional cDFCs). (A) Schematic illustration of bifunctional cDFCs and RBCs. Hemoglobin (Hb) inside RBCs binds oxygen reversibly and changes its absorbance of light. Inspired by RBCs, bifunctional cDFCs enable the rapid measurement of dissolved oxygen concentrations as well as oxygen delivery owing to the encapsulated oxygen indicators. (B) Schematic of the preparation of bifunctional cDFCs *via* Shirasu porous glass membrane emulsification (SPG ME) and evaporation-induced phase separation (EIPS).

COMSOL®. The boundary condition was imported from the actual shapes of cDFCs, reconstructed from CLSM images using Imaris.

Experiments and methods

Materials

The PDMS-TPE (Super-PDMS, XM1700, Fukoku Bussan Co., Ltd, Japan) was a gift from Fukoku Bussan Co., Ltd (Tokyo, Japan). PFOB was gifted by Daikin Industry Co., Ltd (Osaka, Japan). Polyvinyl alcohol (PVA, M_w = 13 000–23 000 kDa, degree of saponification = 87–89 mol%) was purchased from Sigma-Aldrich (St. Louis, USA). Ru(dpp) (Ex/Em = 480 nm/590 nm), PtOEP(Ex/Em = 400 nm/650 nm), and PtTFPP(Ex/Em = 400 nm/650 nm) were purchased from Frontier Scientific Inc. (Newark, USA). Dimethyl sulfoxide (DMSO), sodium hydroxide (NaOH), sodium sulfide (Na_2SO_3), dichloromethane (DCM), high-glucose Dulbecco's modified Eagle's medium (DMEM), fetal bovine serum (FBS), penicillin–streptomycin–amphotericin B suspension (PSA, penicillin – 10 000 IU ml^{-1}, streptomycin – 10 mg ml^{-1}, amphotericin B – 25 μg ml^{-1}), Pt standard solution (996 mg L^{-1}), and phosphate-buffered saline (PBS(−)) were purchased from Wako Pure Chemical Industries, Ltd (Osaka, Japan). Saline was purchased from Otsuka Pharmaceutical Co. Ltd (Tokyo, Japan). Endothelial cell basal medium-2 with bullet kits (EBM-2) was purchased from Lonza Bioscience Ltd (Basel, Switzerland). Human umbilical vein endothelial cells (HUVEC) were purchased from ATCC (Manassas, VA,

USA). Cell counting kit-8 (CCK-8) was purchased from Dojindo Laboratories Co., Ltd (Shiga, Japan).

Preparation of cDFCs and bifunctional cDFCs

An SPG internal pressure module (SPG Technology, Miyazaki, Japan) and hydrophilic SPG membranes (SPG Technology, Miyazaki, Japan) with pore sizes of 4 μm and a membrane working area of 6.3 cm^2 were applied for emulsification. The dispersed phase was composed of 81 μL of PFOB and 2 mL of DCM, which dissolved 80 mg of PDMS-TPE. To prepare bifunctional cDFCs, oxygen probes such as Ru(dpp), PtOEP, or PtTFPP were dissolved in DCM at 0.05 mg mL^{-1} before adding PFOB and PDMS-TPE. The membrane was sonicated in a separate bottle containing a 2 wt% PVA solution for 1 h before emulsification. The SPG membrane emulsification was performed at room temperature for 1 h after immersion in 20 mL of a continuous phase containing 2 wt% PVA in pure water. The transmembrane pressure was adjusted using an external gas-flow controller until the inlet N_2 pressure reached the critical transmembrane pressure (approximately 8 kPa). At this transmembrane pressure, the dispersed phase flux remained constant at 2 mL h^{-1} without fouling. The emulsification was completed after 1 h. Subsequently, the emulsified suspension was stirred for another 2 h to ensure the complete evaporation of DCM. Finally, the resulting suspension was washed sequentially with pure water, ethanol, and water *via* centrifugation. We defined the names of the three prepared bifunctional cDFCs as (i) Ru(dpp)@PFOB/PDMS-TPE, (ii) PtOEP@PFOB/PDMS-TPE, and (iii) PtTFPP@PFOB/PDMS-TPE, respectively.

Size measurement and shape observation of bifunctional cDFCs

The morphology of the dried particles was observed by scanning electron microscopy (SEM) (S4700, Hitachi, Tokyo, Japan). The morphology of the particles in the suspension was observed using a CLSM (FV3000; Olympus, Tokyo, Japan). An Ar laser (514 nm) was used for excitation when the oxygen probes were loaded onto the particles during the SPG ME. The size distribution of the particles in the suspension was measured using a laser diffraction particle size distribution analyzer (LA-950V2; Horiba, Kyoto, Japan).

Phosphoresce intensity measurement

Bifunctional cDFCs were dispersed in water and stirred to form a suspension. For 0% O_2, 1 g of Na_2SO_3 was added to 100 mL of suspension for complete deoxygenation. At 20% O_2, the suspension was saturated with air at room temperature. For 5, 10, and 15% O_2, an N_2/O_2 gas mixer was used to control the perfusion rate of N_2 and O_2 until the DO value was stable in the DO meter (VisiFerm DO ARC 120; Hamilton, Reno, USA) readings. Once the DO concentration stabilized to the intended value, the phosphorescence intensity of the suspension was measured using a spectrofluorometer (FP-8200; JASCO, Japan). The excitation wavelength was 400 nm for PtOEP@PFOB/PDMS-TPE and PtTFPP@PFOB/PDMS-TPE and 500 nm for Ru(dpp)@PFOB/PDMS-TPE, and the emission wavelength was recorded in the range of 500–750 nm for all samples. The Stern–Volmer constant was determined by linear regression using the least-squares method, which is a built-in algorithm from MATLAB 2023a.

Durability evaluation in sterilization processes and long-time incubation in buffer

PtOEP@PFOB/PDMS-TPE and PtTFPP@PFOB/PDMS-TPE suspensions in PBS were used to test particle stability. For the evaluation of durability under cell culture conditions, the particles were suspended in PBS and incubated at 37 °C, 5% CO_2 and 20% O_2 for one week. To evaluate the durability against acidity, 1 mL of suspension was diluted in 20 mL of PBS solution adjusted to pH = 4.4 by adding 1 N HCl, and the resulting suspension was stored for 24 h. For the evaluation of cryopreservation durability, the diluted particle suspension was lyophilized using liquid nitrogen and stored at −30 °C for 7 days. To evaluate sterilization durability, the diluted particle suspension was separately sterilized by autoclaving with ethylene oxide gas (EOG). The particles were washed with PBS after each treatment to remove potentially leeched dyes. The phosphorescence spectrum of each sample was recorded at room temperature under atmospheric conditions. The extent of the oxygen probe leaching was determined using the relative phosphorescence intensity calculated from the samples before and after treatment. The influence of the treatments on the particle morphology was determined by recording SEM images of the samples after treatment. Five samples were collected for each group. Swelling and oxygen probe leaching tests were performed using PtOEP@PFOB/PDMS-TPE and PtTFPP@PFOB/PDMS-TPE suspended in DMEM. The suspension was then incubated at 37 °C under 5% CO_2 and 20% O_2 for one week. The particle size distribution of the suspension was measured daily for one week. A sample was taken from the supernatant and digested in NaOH solution for further analysis of Pt concentration.

Measurement of PtOEP and PtTFPP concentration

The concentrations of PtOEP and PtTFPP in the solution were measured using the atomic absorption spectrometry (AAS) technique. The sample solution was dissolved completely using a NaOH solution (pH = 14) and then filtrated using a 0.22 μm filter membrane. The Pt concentrations in the samples were measured using an atomic absorption spectrometer (ZA3000, Hitachi, Japan). The Pt standard solution was diluted to 125, 62.5, and 25 ppb to obtain a standard calibration curve. Each sample was measured three times with 20 μL amount for each time. The concentrations of the original samples were calculated using the dilution ratios.

Biocompatibility test *in vitro*

The hypoxia-responsive HeLa cells (hr-HeLa cells) were prepared according to our previous research[32] and cultured in 35-mm glass-bottom Petri dishes with high-glucose DMEM supplemented with 10% FBS and 1% PSA at a seeding density of 0.5×10^6 cells per mL. The bifunctional cDFCs were washed with pure water to remove PVA surfactants before being applied

in vitro or *in vivo*. To demonstrate the biocompatibility and phosphorescence response of the bifunctional cDFCs, PtTFPP and PtOEP were dispersed in dishes containing h-HeLa cells at a ratio of 1 : 1. The dishes containing hr-HeLa cells and bifunctional cDFCs were further cultured together in the incubators with 1% O_2 and 20% O_2 separately. Confocal microscopy images of the cells cultured under hypoxic and normoxic conditions were acquired after 48 h. Two lasers (ex = 488 nm and ex = 561 nm) were used to observe hr-HeLa and bifunctional cDFCs, respectively.

To evaluate the cytotoxicity of bifunctional cDFCs, HUVEC were seeded in three 24-well plates with EGM-2 working medium at an initial density of 3.0×10^4 cells per mL and incubated for 24 h under 20% O_2 and 5% CO_2. Subsequently, the bifunctional cDFCs, PtOEP@PFOB/PDMS-TPE, and PtTFPP@PFOB/PDMS-TPE were added to the plates at a concentration of 5% by volume, and equivalent amounts of PtOEP and PtTFPP dissolved in DMSO were added at a concentration of 0.5% by volume as negative controls. Each plate contained blank, control, PtOEP@PFOB/PDMS-TPE, PtTFPP@PFOB/PDMS-TPE, PtTFPP, or PtTFPP (n = 4). Three replicate plates were prepared for the measurements at 24, 48, and 72 h. The cell viability of each well was measured using a microplate reader (ARVO™X3, PerkinElmer, USA) after staining with the CCK-8 reagent following the standard protocol.

Numerical simulation of oxygen release and absorption

The oxygen profiles inside the core–shell particles and microchannel perfusion culture were simulated by the diffusion equation model using the following equation:

$$\frac{\partial C(\vec{r},t)}{\partial t} = D\nabla C(\vec{r},t) \quad (1)$$

The reconstructed CLSM images using Imaris (Imaris version 9.6.0, Bitplane) were used to determine the boundary conditions. The numerical solution was obtained by the finite element method using COMSOL (COMSOL Multiphysics® ver 6.0 software). Initially, one oxygen-saturated PFOB/PDMS-TPE microparticle was immersed in the cell media under hypoxia. Parameters such as oxygen solubility and diffusivity were obtained from the literature.[33,34] All the parameters used in the simulation are summarized in Table S1, ESI.† The MATLAB 2023a software was used to plot the simulation results and other experimental data.

Oxygen sensing of PtOEP@PFOB/PDMS-TPE phosphoresce response to DO change

An aqueous suspension (50 mL) of 1 vol% PtOEP@PFOB/PDMS-TPE was prepared and stirred. The suspension was irradiated with portable UV light (UVGL-58; Analytik Jena, Jena, Germany) at 365 nm in long-wavelength radiation mode. Na_2SO_3 (0.5 g) was then added to the suspension to decrease the DO *via* the following chemical reaction:

$$2Na_2SO_3 + O_2 \rightarrow 2Na_2SO_4$$

The video was recorded under UV light irradiation for 2 min after the addition of Na_2SO_3.

Statistical analysis

Statistical tests were performed for cell viability using one-way analysis of variance (ANOVA). Differences were considered statistically significant at $p < 0.05$.

Results and discussion

The effect of oxygen probe loading on the size and shape of cDFCs

As discussed in our previous studies, SPG ME is an efficient technology for producing uniform core–shell microparticles with three phases (organic, aqueous, and PFC).[17] Monodisperse PFOB/PDMS-TPE core–shell microparticles as cDFCs were prepared using the SPG-ME method, followed by EIPS (Fig. 2(A)). PDMS-TPE has excellent oxygen permeability and light transmittance, which are optimal for both the oxygen carrier shell and the oxygen sensor substrate. Therefore, oxygen probes were incorporated into the latest cDFC and PFOB/PDMS-TPE microcapsules. With the addition of Ru(dpp), PtOEP, and PtTFPP to the dispersed phase, the resulting bifunctional cDFCs formed the same concave shape as normal cDFCs (Fig. 2(A)). The spontaneous concave shape is an important feature of the PDMS-TPE-based cDFCs found in our previous study.[17] This is probably because the addition of the oxygen probe was considerably low and the particle morphology was unaffected. Compared to the size distributions of bifunctional and normal cDFCs, which are co-plotted in Fig. 2(B), the monodispersities of the particles were not affected by the loading of oxygen probe molecules. The average sizes of PFOB/PDMS-TPE, Ru(dpp)@PFOB/PDMS-TPE, PtOEP@PFOB/PDMS-TPE and PtTFPP@PFOB/PDMS-TPE were all close to the typical diameter of human RBCs (approximately 8 μm).[35]

Difference of the loading amount of three oxygen probes to cDFCs

Confocal microscopy images of different metalloporphyrin-loaded PFOB/PDMS-TPE suspensions under hypoxia (5% O_2) were obtained to confirm the presence and functionality of the oxygen probes. The three core–shell microparticles exhibited red phosphorescence in their shells: Ru(dpp) @PFOB/PDMS-TPE, PtTFPP@PFOB/PDMS-TPE, and PtOEP@PFOB/PDMS-TPE (Fig. 2(C)).

Metalloporphyrin oxygen probes are hydrophilic, hence they were encapsulated by PDMS-TPE owing to EIPS and 'like-dissolve-like' principle.[36,37] However, Ru(dpp) is a chloride salt that undergoes hydrolysis in the continuous phase during emulsification, decreasing its encapsulation ratio.[38] Moreover, the agglomeration caused by the poor solubility of Ru (dpp) in PDMS-TPE and the net charge of the $Ru(dpp)_3^{2+}$ ions might have led to a higher photobleaching rate,[39] further contributing to the weakest phosphorescence intensity observed in the confocal microscopic images. Because of the similar physical and chemical properties of PtTFPP and PtOEP, the PtTFPP-encapsulated samples showed relatively low phosphorescence in confocal microscopy images under hypoxia, likely owing to their relatively low quantum yields.[40] In addition, the lowest

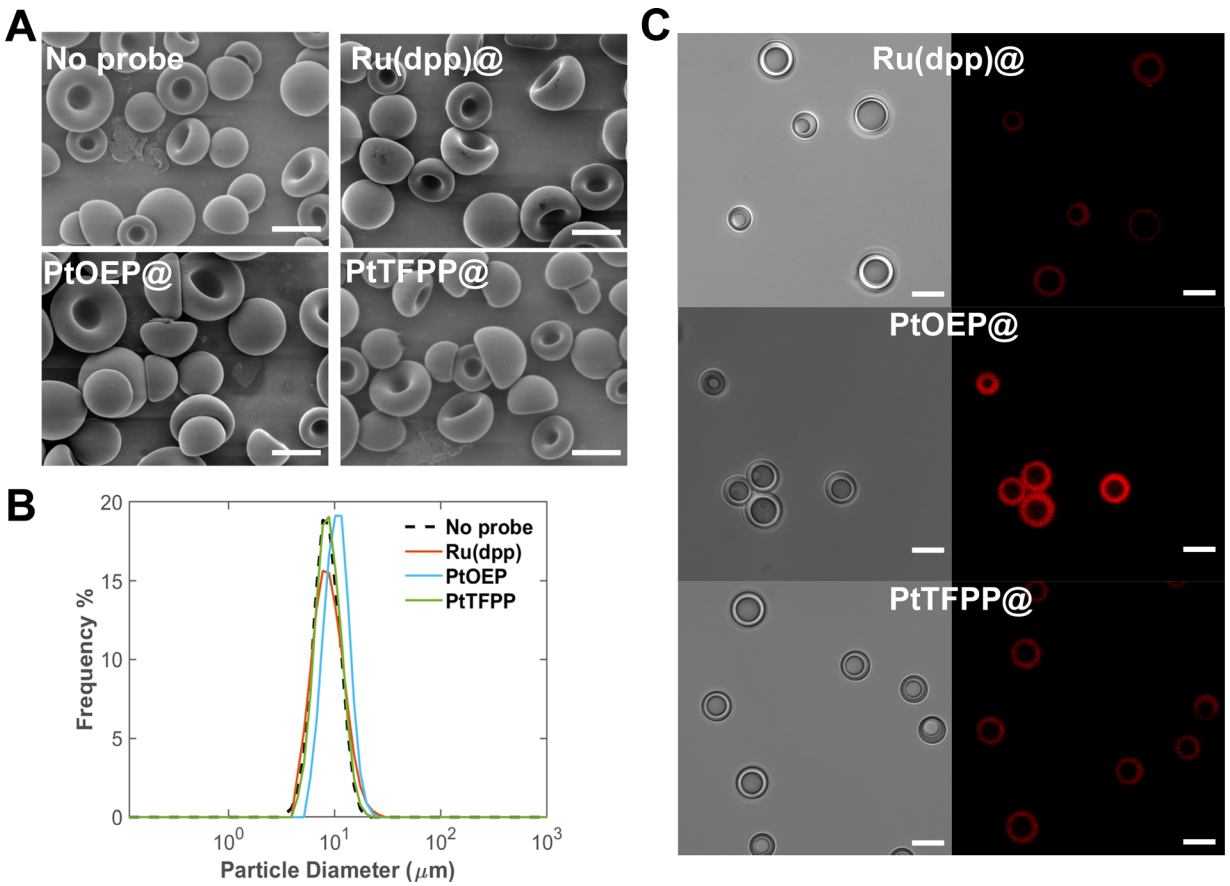

Fig. 2 Characterization of bifunctional cDFCs and normal cDFCs PFOB/PDMS-TPE. (A) SEM images; scale bar = 10 μm. (B) Size distribution, diameter of PFOB/PDMS-TPE, Ru(dpp)@PFOB/PDMS-TPE, PtOEP@PFOB/PDMS-TPE and PtTFPP@PFOB/PDMS-TPE are 8.4 ± 2.6, 8.5 ± 3.0, 9.9 ± 2.6, and 8.3 ± 2.3 μm, respectively. (C) Confocal microscopic images under 5% O_2; red channel: ex = 561 nm; scale bar = 10 μm.

possible amount of oxygen probe was added to the dispersed phase to prevent the aggregation of the unencapsulated oxygen probes on the particle surface. Otherwise, the additional charges induced by the complex on the particle surface caused aggregation in the PBS solution.

Furthermore, the different hydrophobicities of the three oxygen probes caused discrepancies in the resulting encapsulation ratios of the PDMS-TPE shell. Initially, 2 mL of a dispersed phase contained 0.1 mg of PtOEP or PtTFPP, which was equivalent to 26.8 and 16.7 μg, respectively. After the particles were digested using NaOH and diluted 1000 times, the Pt concentrations in PtOEP@PFOB/PDMS-TPE and PtTFPP@PFOB/PDMS-TPE were measured as 3.61 and 3.26 ppb using the AAS analysis, respectively. The calculated encapsulation efficiencies of the emulsified bifunctional cDFCs are 26.9% and 39.0% for PtOEP and PtTFPP, respectively. These values are equal to or greater than those reported in other studies using a polymer matrix to encapsulate PtOEP or PtTFPP in the form of microparticles or nanoparticles.[28,30,41,42] Comparing the chemical structures of PtOEP and PtTFPP, the presence of four extra substituted phenyl groups rendered PtTFPP more hydrophobic (lipophilic) than PtOEP, contributing to its higher compatibility with PDMS-TPE. A relatively high loading efficiency was also achieved because TPE was used without the need for an additional crosslinking process, as several studies have reported that the high temperature of the curing process affects the loading efficiency of oxygen probes.[43–45]

Phosphorescence sensitivity and response of cDFCs to dissolved oxygen

The three bifunctional cDFCs exhibited different phosphorescence intensities in response to the same oxygen concentration (Fig. 2(C)). However, to evaluate their sensing abilities, it is important to determine their sensitivity to different oxygen concentrations.

Considering that the oxygen concentration varies from 21% as inhaled air enters the lungs to approximately 5% in venous blood and even 1% in some tissues,[2] a range of 0% to 20% oxygen was selected as the test range for bifunctional cDFCs to examine their performance and sensitivity.

Ru(dpp)@PFOB/PDMS did not exhibit strong intensity peaks, and a clear separation of peaks between normoxia and hypoxia was observed in the phosphorescence intensity map (Fig. S1, ESI†). Consistent with the poor performance observed in the confocal microscopy images, PDMS-TPE did not appear to be a good matrix for Ru(dpp) encapsulation.

Phosphorescence maps of PtOEP@PFOB/PDMS-TPE are shown in Fig. 3(A) and (B). Both were excited by the emission

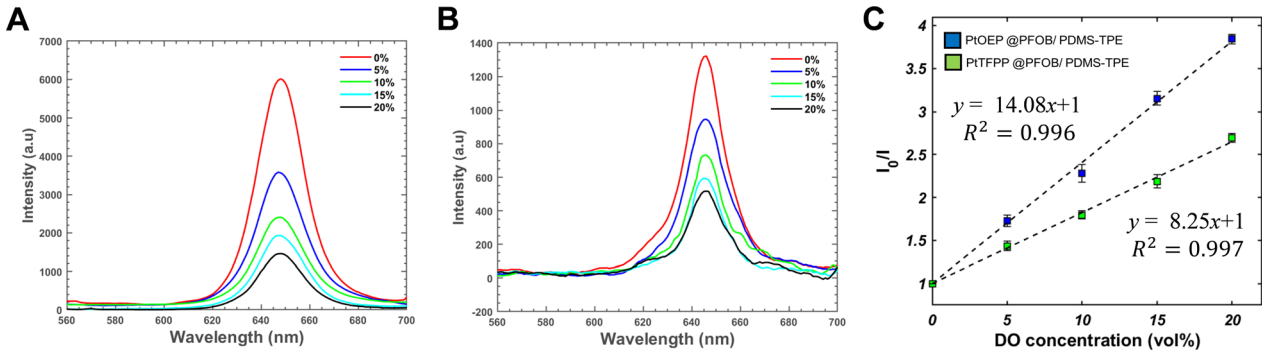

Fig. 3 Phosphorescence response of bifunctional cDFCs to different DO values, representing the percentage of O_2 in the mixture of N_2 and O_2; (A) intensity map of PtOEP@PFOB/PDMS-TPE; (B) intensity maps of PtTFPP@PFOB/PDMS-TPE; (C) co-plot of their corresponding Stern–Volmer plots, K_m values are 14.08 (PtOEP@PFOB/PDMS-TPE) and 8.25 (PtTFPP@PFOB/PDMS-TPE).

peaks at approximately 650 nm. This emission wavelength was close to the literature values for pure PtOEP and PtTFPP,[46] implying that no apparent Stokes shift was observed owing to encapsulation. In contrast, PtTFPP@PDMS-TPE exhibits lower absolute intensities than PtOEP@PDMS-TPE at all wavelengths. Because the phosphorescence mechanism is an intramolecular deactivation process, the Stern–Volmer relationship (eqn (2))[47] was used to describe the phosphorescence quenching kinetics of the oxygen probes. The Stern–Volmer constant, or the overall quenching constant, K_{SV} represents the sensitivity of a sensor. Fig. 3(C) shows the intensity data transformed from Fig. 3(A) and (B) with their linear correlation. Both bifunctional cDFCs fit Stern–Volmer kinetics well, with R^2 values close to 1. The slopes of the plots, K_{SV}, were obtained for PtOEP and PtTFPP.

$$\frac{I_0}{I} = 1 + K_{SV} \cdot [O_2] \quad (2)$$

Because of the low quantum yield of PtTFPP, both the overall phosphorescence intensity and K_{SV} of the PtTFPP-loaded sample were lower than those of the PtOEP-loaded sample. In addition, the cost of PtTFPP is generally higher than that of PtOEP owing to its complex synthesis.[19] Therefore, regarding bifunctional oxygen carriers, PtOEP is considered the most suitable oxygen probe among the three candidates, and PtTFPP could be a potential alternative. In contrast, Ru(dpp) was not considered a suitable oxygen probe for the PFOB/PDMS-TPE oxygen carriers because it could not determine the exact DO concentration based on its phosphorescence intensity after encapsulation.

Durability and sterilization of the bifunctional cDFCs

The stability tests mainly focused on the protectivity offered by the PDMS-TPE shell under certain probable treatments. The results shown in Fig. 4(A) demonstrate the ability of bifunctional cDFCs to withstand different environments and treatments. First, both PDMS and PDMS dispersed in PBS at 37 °C show negligible degradation in their phosphorescence intensity after 2 weeks. Owing to the chemical stability of the PDMS-based shell, no significant change in their size and shape is observed after immersion in an acidic solution at pH = 4.4 (Fig. S2, ESI†), indicating that the bifunctional cDFCs can withstand even the extremely acidic conditions in inflammatory tissues. A certain degree of reduction in luminescence was observed after freezing. Among the two sterilization methods, autoclaving of the particles led to the partial melting and breaking of the PDMS-TPE shell, as shown in Fig. 4(A) and Fig. S2 (ESI†), owing to the high temperature and pressure. Thus, the phosphorescence intensities of both bifunctional cDFCs were significantly reduced by the leaching of PtOEP and PtTFPP. In comparison, the EOG method is milder; therefore, the morphology of the sterilized particles is not altered, thereby maintaining the phosphorescence intensity after treatment. Hence, except for autoclave treatment, bifunctional cDFCs can withstand low-temperature, acidic, and normal environments without breaking the shell, owing to the stability of PDMS-TPE.

Stable loading of oxygen probes in the bifunctional cDFCs

Oxygen-probing molecules are released from their matrices either because of the destruction of the matrices or passive diffusion. Leaching of oxygen probes causes the loss of bifunctional cDFCs and toxicity to the surrounding organisms. Therefore, understanding the leaching mechanisms of bifunctional cDFCs is necessary to ensure their long-term use.

The mass ratio of the oxygen probes to PDMS-TPE in the original dispersed phase was controlled at 1 : 800, which is a typical value for loading metalloporphyrins onto polymeric substrates at the microscale.[29,45,48] As discussed in the previous section, the encapsulation efficiencies of PtOEP and PtTFPP were ~30%. The percentage of PtOEP or PtTFPP released was determined by measuring the Pt concentration in the supernatant at different times. Fig. 4(C) shows the cumulative percentages of PtOEP and PtTFPP released from the bifunctional cDFCs incubated in DMEM over time based on the AAS results. The leaching of both PtOEP and PtTFPP from the PDMS-TPE matrix was insignificant (as low as approximately 1%). Moreover, no obvious increase in the leaching rates of either oxygen probe was observed during the one-week incubation period. We believe that leaching of the loaded probe from the bifunctional cDFCs was minimized.

In addition, the results of the stability, swelling, and release tests showed that the PDMS-TPE shell was stable during incubation in DMEM. Depending on the strong hydrophobic

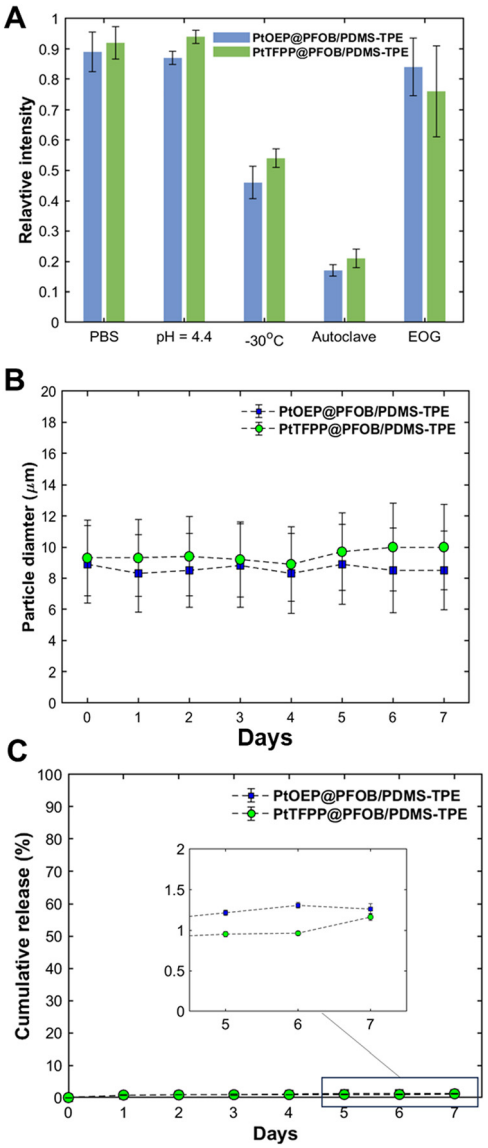

Fig. 4 Stability and leaching test of PtOEP@PFOB/PDMS-TPE and PtTFPP@PFOB/PDMS-TPE; (A) phosphorescence reduction after treatment. (B) Swelling test of particles in DMEM at 37 °C for one week. (C) Oxygen probe releasing in DMEM at 37 °C for one week; the details from day 5 to day 7 are magnified in the inset plot.

nature of the organic metal complexes, the release of PtOEP and PtTFPP is expected to be considerably slower by simple molecular diffusion. From the particle size data for each day, shown in Fig. 4(B), both PtOEP@PFOB/PDMS-TPE and PtTFPP@PFOB/PDMS-TPE exhibited negligible swelling behavior in terms of diameter. The size distribution error was maintained at approximately 30%, which is typical of SPG ME.[49–52] These results indicated that the PDMS-TPE shell did not swell in the cell culture media for a long time. Moreover, the impermeability of water to the PDMS-TPE shell prevented the quenching of the dyes by hydroxyl vibrations.[53]

The bifunctional cDFCs exhibited resistance to several treatments and long-term incubation, demonstrating their potential to function for a long time in cell cultures and bioreactors.

Biocompatibility of the bifunctional cDFCs

Ideal substrate matrices for AOCs and oxygen sensors have several advantages such as oxygen permeability, biocompatibility, chemical inertness, and good dispersity in the culture medium. Thus, two cell lines were used to quantitatively and visually examine the biocompatibility of the bifunctional cDFCs. As an indicator of a cellular hypoxic environment in our previous studies,[9,17] hr-HeLa cells showed low oxygen concentrations based on the expression of green fluorescence.[32] In addition, the bifunctional cDFCs emitted red phosphorescence. Both luminescence intensities were inversely proportional to the DO concentration (Fig. 3). As the emission wavelengths of both PtTFPP and PtOEP were considerably different from those of hr-HeLa cells, neither cells nor particles were dual-labelled with green and red colors (Fig. 5(A)). PtOEP@PFOB/PDMS-TPE and PtTFPP@PFOB/PDMS-TPE microparticles were attached to h-HeLa cells without damaging them. Furthermore, because confocal microscopy images were captured at the same *z*-position, none of the particles indicated by red phosphorescence overlapped with the hr-HeLa cells. This demonstrated that the micro-sized cDFCs were not taken up by the hr-HeLa cells.

In contrast, under normoxic conditions, both bifunctional cDFCs and hr-HeLa cells exhibited considerably weaker fluorescence than under hypoxic conditions (as depicted in the merged channel images in Fig. S3, ESI†). This indicated that both hr-HeLa cells and bifunctional cDFCs were able to reflect the actual local hypoxic area *in vitro*.

Phosphorescent dyes, such as PtOEP and PtTFPP, can generate highly reactive singlet oxygen species and thus usually have a certain degree of phototoxicity.[54–56] Therefore, encapsulation of these dyes into a biocompatible matrix is important for eliminating dye damage. We tested our bifunctional cDFCs with HUVEC, which have a relatively low oxygen consumption rate,[57] to minimize the effect of oxygen delivery from bifunctional cDFCs on cell viability.

As shown in Fig. 5(C), the PtOEP@PFOB/PDMS-TPE-and PtTFPP@PFOB/PDMS-TPE-dispersed wells exhibited high cell viability compared to the control groups on each day. In contrast, the pure PtOEP- and PtTFPP-added wells were cytotoxic to HUVEC, indicating the toxicity of the Pt complex in the cell culture medium. Although 0.5% DMSO was found to be the maximum concentration tolerated by some cell lines, the cytotoxicity could[58,59] still be partially attributed to organic solvent effects. However, PtOEP and PtTFPP did not disperse in the cell culture medium, making them unsuitable for use alone. In contrast, bifunctional cDFCs were evenly dispersed around HUVEC without DMSO (Fig. 5(B)), without damage to the cells or cell internalization. Therefore, it is desirable to encapsulate oxygen probes into biocompatible substrate matrices such as PDMS-TPE. With the protection of the PDMS-TPE shell, photobleaching and light attenuation effects caused by the interaction of oxygen-sensing probes with biological samples under a microscope should be avoided.[20]

3D Numerical prediction of oxygen transport of cDFCs based on their measured shape

To achieve real-time sensitivity of bifunctional cDFCs, we need to clarify how fast the oxygen in the particle reaches equilibrium with its environment and whether the oxygen transfer process is

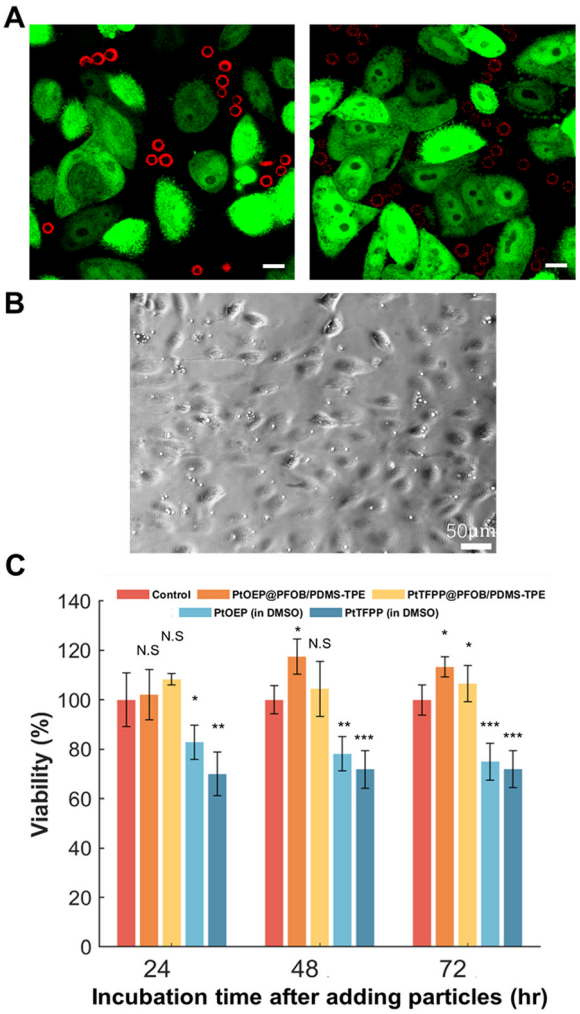

Fig. 5 Biocompatibility of bifunctional cDFCs: (A) confocal microscopic images of Hr-HeLa cells (green) cultured with bifunctional cDFCs (red, left: PtOEP@PFOB/PDMS-TPE, right: PtTFPP@PFOB/PDMS-TPE) under 5% O_2; red channel: ex = 561 nm, green channel: ex = 488 nm; scale bar = 10 μm. (B) Optical microscopic image of HUVEC cultured with PtOEP@PFOB/PDMS-TPE. (C) Cell viability results of bifunctional cDFCs tested by HUVEC at 24, 48, and 72 h; *: $p < 0.05$, **: $p < 0.01$, ***: $p < 0.001$.

the rate-limiting step. Thus, we studied the transport of oxygen inside a core–shell PFOB/PDMS-TPE interacting with the oxygen change outside. We started with a spherical geometry with a core–shell structure (Fig. S4A, ESI†). With a particle diameter of 8 μm equivalent to the human RBC, the profile of the change of oxygen inside the particle was simulated as it was put in the bulk with hypoxia. As illustrated in the time course of the 2D oxygen map (Fig. S4B, ESI†), the spherical core–shell PFOB/PDMS-TPE microparticles release oxygen in an axis-symmetrical pattern, which varies only according to the *r*-axis.

As shown in Fig. 6(A), the microparticles immediately released oxygen from their PFOB core through the PDMS-TPE shell to the surrounding region until the internal and external oxygen concentrations were balanced. This simulation process was rapid because of the high oxygen permeability of the PDMS-TPE material. The oxygen concentration inside the particle pore decreased from 5 mM to 0.5 mM within 10 ms, indicating that the major oxygen releasing period was considerably short. The typical oxygen diffusion time through an RBC cell was approximately 10 ms in a previous study.[60] The diffusion time of the spherical PFOB/PDMS-TPE microparticles, calculated according to the characteristic time of diffusion[61] shown in eqn (3), was approximately 8.5 ms, which was approximately equal to or even shorter than that of the RBC. In other words, the core–shell PFOB/PDMS-TPE microspheres quickly responded to local oxygen concentration changes, and their high permeability allowed them to detect and deliver oxygen to the cells without any lag.

$$\tau = \frac{R^2}{D} \quad (3)$$

However, compared with spherical particles, cDFCs have a unique concave shape with a core–shell structure, as shown in Fig. 2(A). To better understand the oxygen distribution through the cDFCs, we captured the geometric features of the RBC-like shapes in our single-particle oxygen transfer model. A series of images were captured using confocal laser scanning microscopy for a typical cDFC stained with Nile red. As shown in Fig. S5, ESI,† the *z*-stack of confocal microscopic images of a typical concave PFOB/PDMS-TPE microparticle is then reconstructed to visualize the 3D structure of the cDFC using an image-stacking software, IMARIS. We then obtained the cross-section of the cDFC at the *x*–*z* or *y*–*z* planes by cutting the stacked three-dimensional (3D) confocal image. By importing 2D cross-sectional images of the cDFC particles into COMSOL and revolving the 2D contour on its central axis, we successfully built a 3D geometric model of our cDFC based on axial symmetry. Consequently, a 3D concave PFOB/PDMS-TPE core–shell microparticle model was established, as shown in Fig. 6(B).

Finally, we successfully simulated the oxygen concentration inside a microsized PFOC with a concave shape (Fig. 6(B)). Using methods similar to the 3D spherical model, we plotted the time course of the oxygen profile variation in both 2D and 3D images. The release of oxygen from the cDFC core occurred rapidly across the shell (Fig. 6(C)). Because the material properties and boundary conditions of the cDFC model were almost identical to those of the previous spherical model, we investigated the effect of AOC geometry by comparing the simulated oxygen transfer time courses of the spherical and concave morphologies (Fig. S4, ESI† and Fig. 6). Compared with the spherical PFOB/PDMS-TPE model, cDFCs released oxygen slightly faster than DFC, as indicated by the saturation curve shown in Fig. 6(D), owing to the higher surface area of cDFCs than that of DFCs. The effect of inner convection,[8] which has been reported for RBCs, was not considered in this study. Thus, its performance is better than that of this calculation. We expect the cDFCs and bifunctional cDFCs to be efficient for oxygen delivery and sensing.

In situ detection of hypoxia by the phosphorescence change of bifunctional cDFCs

Owing to the excellent transparency of the PDMS-TPE cells and the high quantum yield of PtOEP, the change in DO can be

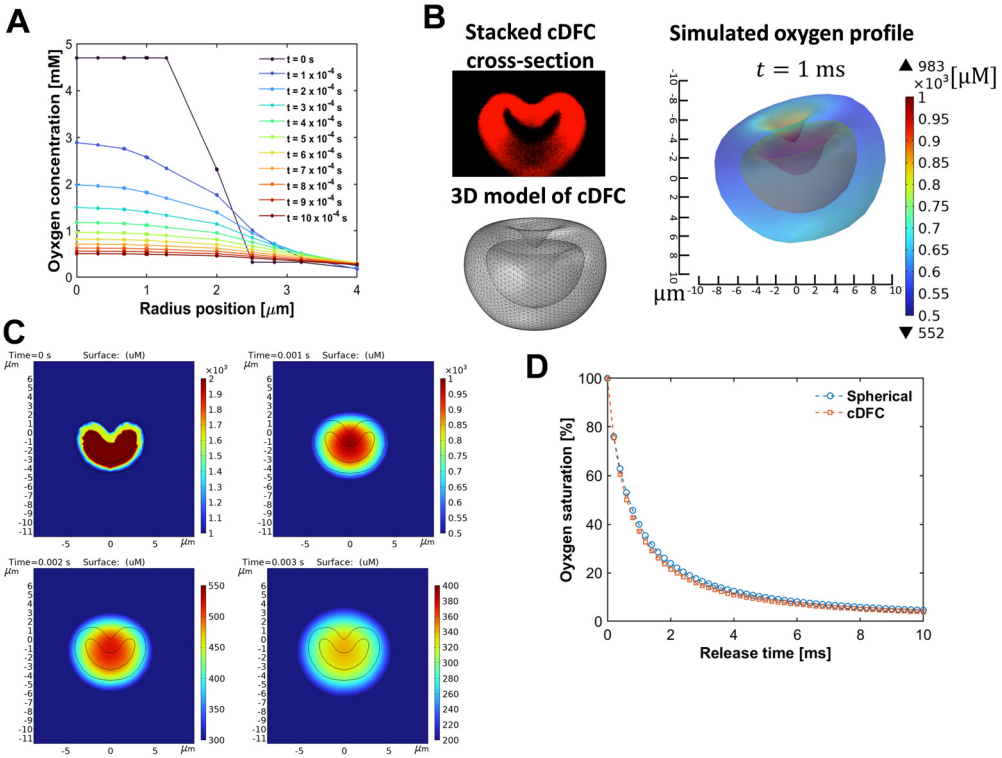

Fig. 6 Simulation results of oxygen release from PFOB/PDMS-TPE spherical microparticles and concave microparticles, cDFCs: (A) average oxygen concentration distributed along the radius of spherical PFOB/PDMS-TPE microparticles at different times; (B) 3D model of cDFC and simulated 3D oxygen distribution; (C) cross-sections of the simulated 3D oxygen diffusion profile of cDFC at different time points; (D) comparison of oxygen release rate of spherical PFOB/PDMS-TPE and cDFC.

visualized under UV radiation, as observed by the strong phosphorescence emitted by the bifunctional cDFCs under hypoxia produced by chemical oxygen consumption. After adding Na_2SO_3 to the suspension of PtOEP@PFOB/PDMS-TPE, the time course of the color change in the suspension was observed (Fig. 7 and Fig. S6, ESI†). Because of the high oxygen permeability of PDMS-TPE, the PFOB/PDMS-TPE microparticles dynamically released oxygen, which reacted with Na_2SO_3. Based on the mathematical simulation of the oxygen transfer of single-core–shell PFOB/PDMS-TPE microparticles, we showed the quick response of the oxygen profile inside the oxygen carrier to a sudden oxygen change in the surroundings. Hence, the bifunctional cDFCs immediately achieved equilibrium with DO in the bulk phase by releasing oxygen from their cores, which did not cause any lag in the oxygen quenching of the oxygen probes embedded in the particle shell. The time interval of the phosphorescence augmentation can then be attributed to the reaction of Na_2SO_3 and the response time of the bifunctional cDFCs. Because excessive Na_2SO_3 allowed the solution to remain without DO for some time after the initial DO had reacted completely, we were able to estimate the lifetime of our bifunctional cDFCs based on phosphorescence decay. Fig. 7(B) shows that the phosphorescence lasted for at least 70 s without any decay, which is a rough reference for the lifetime of PtOEP@PFOB/PDMS-TPE.

The bifunctional cDFCs had a considerably high oxygen capacity and oxygen diffusivity owing to the presence of PFOB in the core and efficiently exchanged oxygen once DO was consumed by the cells. Because the oxygen solubility in both PDMS-TPE and PFOB is linearly dependent on the local oxygen concentration and obeys Henry's law,[33] bifunctional cDFCs could serve as excellent ratiometric DO sensors without the need for complex calibration. Bifunctional cDFCs can monitor and reflect the oxygen content without disturbing the culture environment. This capability could prove invaluable for maintaining optimal oxygen concentrations during the expansion and perfusion cultures of cells in tissue engineering in the future.

Conclusions

Inspired by RBCs, we developed a new bifunctional artificial oxygen carrier, bifunctional cDFCs, by loading Ru(dpp), PtOEP, and PtTFPP into PFOB/PDMS-TPE core–shell microparticles without affecting the size, morphology, and monodispersity of the oxygen carriers. The resulting concave microsized oxygen carriers ratiometrically indicated the surrounding oxygen levels. Among the three oxygen probes, PtOEP was considered the most appropriate for PFOB/PDMS-TPE because of its excellent sensitivity, phosphorescence intensity, biocompatibility, and stability. Both experimental visualization and numerical simulation indicated the quick response and long lifetime of bifunctional cDFCs to local hypoxia. Hence, these

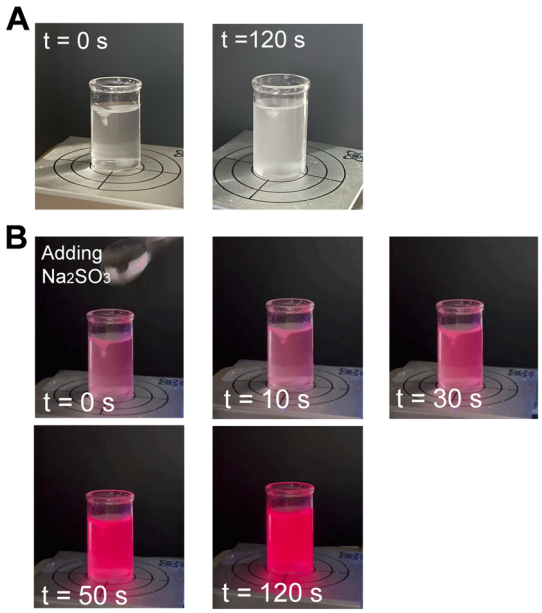

Fig. 7 Hypoxia response rate of the suspension containing 1 vol% of PtOEP@PDMS-TPE in water. The hypoxia condition was mimicked by the oxygen consumption of the chemical reaction: $2Na_2SO_3 + O_2 \rightarrow 2Na_2SO_4$. (A) No phosphorescence was observed without UV irradiation ever after the addition of Na_2SO_3. (B) Phosphorescence rapidly appeared with UV irradiation at 365 nm after the addition of Na_2SO_3.

erythrocyte-mimetic bifunctional cDFCs represent a potentially controlled oxygenation approach for various tissue-engineering applications.

Author contributions

Q. Z.: experiments and writing, N. F. I.: writing, and T. I.: research planning, supervision, and writing.

Conflicts of interest

There are no conflicts to declare.

Acknowledgements

We gratefully acknowledge Fukoku Bussan Co., Ltd for providing PDMS-TPE (Super-PDMS, XM1700) and Daikin Industries, Ltd for providing PFOB. We appreciate for the insightful discussions with Mr. Tomohito Hamada, Dr. Shigehito Sagisaka, and Mr. Yousuke Kishikawa for this study. This work was financially supported by Daikin Industries, Ltd, JSPS Kakenhi (Kaitaku, Grant number: 22K18311), and a Ministry of Education, Culture, Sports, Science, and Technology (MEXT) scholarship from the Japanese Government for Qiming Zhang.

References

1 H. Sakai, K. Sou, H. Horinouchi, K. Kobayashi and E. Tsuchida, *Artif. Organs*, 2009, **33**, 139–145.
2 E. Ortiz-Prado, J. F. Dunn, J. Vasconez, D. Castillo and G. Viscor, *Am. J. Blood Res.*, 2019, **9**, 1–14.
3 E. C. Finger and A. J. Giaccia, *Cancer Metastasis Rev.*, 2010, **29**, 285–293.
4 M. L. Ellsworth, T. Forrester, C. G. Ellis and H. H. Dietrich, *Am. J. Physiol.: Heart Circ. Physiol.*, 1995, **269**, H2155–H2161.
5 A. Jubran, *Crit. Care*, 1999, **3**, R11.
6 M. Ozekinci, E. Kucuksayan, G. Erdogan, M. Aslan, E. Pestereli, M. Canpolat and A. Sircan-Kucuksayan, *Biotech. Histochem.*, 2020, **95**, 203–209.
7 M. Radisic, J. Malda, E. Epping, W. Geng, R. Langer and G. Vunjak-Novakovic, *Biotechnol. Bioeng.*, 2006, **93**, 332–343.
8 M. Radisic, W. Deen, R. Langer and G. Vunjak-Novakovic, *Am. J. Physiol.: Heart Circ. Physiol.*, 2005, **288**, H1278–H1289.
9 X. Fu, S. Ohta, T. Kawakatsu, M. Kamihira, Y. Sakai and T. Ito, *Adv. Mater. Technol.*, 2022, **7**, 2100573.
10 A. Wrobeln, J. Laudien, C. Groß-Heitfeld, J. Linders, C. Mayer, B. Wilde, T. Knoll, D. Naglav, M. Kirsch and K. B. Ferenz, *Eur. J. Pharm. Biopharm.*, 2017, **115**, 52–64.
11 H.-Y. Lee, H.-W. Kim, J. H. Lee and S. H. Oh, *Biomaterials*, 2015, **53**, 583–591.
12 H. Z. An, E. R. Safai, H. Burak Eral and P. S. Doyle, *Lab Chip*, 2013, **13**, 4765.
13 X. Fu, S. Ohta, M. Kamihira, Y. Sakai and T. Ito, *Langmuir*, 2019, **35**, 4094–4100.
14 Y. T. Lai, M. Sato, S. Ohta, K. Akamatsu, S. Ichi Nakao, Y. Sakai and T. Ito, *Colloids Surf., B*, 2015, **127**, 1–7.
15 L.-Y. Chu, R. Xie, J.-H. Zhu, W.-M. Chen, T. Yamaguchi and S. Nakao, *J. Colloid Interface Sci.*, 2003, **265**, 187–196.
16 K. Nakakubo, H. Inoue, H. Yoshioka, K. Morita, T. Kotani and Y. Oki, in *Optical Components and Materials XVIII*, ed. M. J. Digonnet and S. Jiang, SPIE, 2021, p.17.
17 Q. Zhang, N. F. Inagaki, H. Yoshida, M. Kamihira, Y. Sakai and T. Ito, *J. Membr. Sci.*, 2024, **689**, 122119.
18 X. Wang and O. S. Wolfbeis, *Chem. Soc. Rev.*, 2014, **43**, 3666–3761.
19 E. W. Baker, J. William Louda and W. L. Orr, *Org. Geochem.*, 1987, **11**, 303–309.
20 M. Quaranta, S. M. Borisov and I. Klimant, *Bioanal. Rev.*, 2012, **4**, 115–157.
21 C.-S. Chu, Y.-L. Lo and T.-W. Sung, *Talanta*, 2010, **82**, 1044–1051.
22 C.-S. Chu, Y.-L. Lo and T.-W. Sung, *Photonic Sens.*, 2011, **1**, 234–250.
23 M. Pollack, P. Pringsheim and D. Terwoord, *J. Chem. Phys.*, 1944, **12**, 295–299.
24 C. S. Burke, J. P. Moore, D. Wencel, A. K. McEvoy and B. D. MacCraith, *J. Biomed. Opt.*, 2008, **13**, 014027.
25 Y.-E. Koo Lee, E. E. Ulbrich, G. Kim, H. Hah, C. Strollo, W. Fan, R. Gurjar, S. Koo and R. Kopelman, *Anal. Chem.*, 2010, **82**, 8446–8455.
26 S. Schreml, R. J. Meier, O. S. Wolfbeis, T. Maisch, R. Szeimies, M. Landthaler, J. Regensburger, F. Santarelli, I. Klimant and P. Babilas, *Exp. Dermatol.*, 2011, **20**, 550–554.
27 W. Rumsey, J. Vanderkooi and D. Wilson, *Science*, 1988, **241**, 1649–1651.

28 X.-H. Wang, H.-S. Peng, H. Ding, F.-T. You, S.-H. Huang, F. Teng, B. Dong and H.-W. Song, *J. Mater. Chem.*, 2012, **22**, 16066.
29 L. Liang, G. Li, Z. Mei, J. Shi, Y. Mao, T. Pan, C. Liao, J. Zhang and Y. Tian, *Anal. Chim. Acta*, 2018, **1030**, 194–201.
30 P. Ashokkumar, N. Adarsh and A. S. Klymchenko, *Small*, 2020, **13**, 2002494.
31 N. E. Stankova, P. A. Atanasov, Ru. G. Nikov, R. G. Nikov, N. N. Nedyalkov, T. R. Stoyanchov, N. Fukata, K. N. Kolev, E. I. Valova, J. S. Georgieva and St. A. Armyanov, *Appl. Surf. Sci.*, 2016, **374**, 96–103.
32 A. Ono, A. Ito, T. Sato, M. Yamaguchi, T. Suzuki, Y. Kawabe and M. Kamihira, *J. Biosci. Bioeng.*, 2017, **124**, 115–124.
33 J. Jägers, A. Wrobeln and K. B. Ferenz, *Pflugers Arch*, 2021, **473**, 139–150.
34 I. Miranda, A. Souza, P. Sousa, J. Ribeiro, E. M. S. Castanheira, R. Lima and G. Minas, *J. Funct. Biomater.*, 2021, **13**, 2.
35 J. Ford, *Int. J. Lab. Hematol.*, 2013, **35**, 351–357.
36 D. T. Pham, A. Chokamonsirikun, V. Phattaravorakarn and W. Tiyaboonchai, *J. Mater. Sci.*, 2021, **56**, 2016–2036.
37 Y. H. Yuan, Q. Ma, Y. Song, M. Y. H. Tang, Y. K. Chan and H. C. Shum, *Macromol. Chem. Phys.*, 2017, **218**, 1600422.
38 B. Limburg, E. Bouwman and S. Bonnet, *Coord. Chem. Rev.*, 2012, **256**, 1451–1467.
39 K. Presley, J. Hwang, S. Cheong, R. Tilley, J. Collins, M. Viapiano and J. Lannutti, *Mater. Sci. Eng., C*, 2017, **70**, 76–84.
40 Y. Qiao, T. Pan, J. Li, C. Yang, J. Wen, K. Zhong, S. Wu, F. Su and Y. Tian, *Appl. Sci.*, 2019, **9**, 4404.
41 X.-H. Wang, H.-S. Peng, W. Yang, Z.-D. Ren, X.-M. Liu and Y.-A. Liu, *J. Mater. Chem. B*, 2017, **5**, 1856–1862.
42 S.-Y. Hwang, D. Song, E.-J. Seo, F. Hollmann, Y. You and J.-B. Park, *Sci. Rep.*, 2022, **12**, 9397.
43 Q. Wang, J.-M. Zhang and S. Li, *Instrum. Sci. Technol.*, 2019, **47**, 19–50.
44 S. Dash, S. Mishra, S. Patel and B. K. Mishra, *Adv. Colloid Interface Sci.*, 2008, **140**, 77–94.
45 R. Xue, P. Behera, J. Xu, M. S. Viapiano and J. J. Lannutti, *Sens. Actuators, B*, 2014, **192**, 697–707.
46 Y. Amao and I. Okura, *J. Porphyrins Phthalocyanines*, 2009, **13**, 1111–1122.
47 M. H. Gehlen, *J. Photochem. Photobiol., C*, 2020, **42** 100338.
48 J. Prasad, A. Joshi, R. D. Jayant and R. Srivastava, *Biotechnol. Bioeng.*, 2011, **108**, 2011–2021.
49 E. Kakazu, T. Murakami, K. Akamatsu, T. Sugawara, R. Kikuchi and S. Nakao, *J. Membr. Sci.*, 2010, **354**, 1–5.
50 D. Bao, H. Zhang, X. Liu, Y. Zhao, X. Ma and Q. Yuan, *J. Dispersion Sci. Technol.*, 2007, **28**, 485–490.
51 K. Akamatsu, Y. Ikeuchi, A. Nakao and S. Nakao, *J. Colloid Interface Sci.*, 2012, **371**, 46–51.
52 Y. T. Lai, S. Ohta, K. Akamatsu, S. I. Nakao, Y. Sakai and T. Ito, *Biotechnol. Prog.*, 2015, **31**, 1676–1684.
53 R. N. Gillanders, M. C. Tedford, P. J. Crilly and R. T. Bailey, *Anal. Chim. Acta*, 2004, **502**, 1–6.
54 I. J. Macdonald and T. J. Dougherty, *J. Porphyrins Phthalocyanines*, 2001, **05**, 105–129.
55 J. Zhang, F. Cheng, J. Li, J.-J. Zhu and Y. Lu, *Nano Today*, 2016, **11**, 309–329.
56 R. Bonnett, R. D. White, U. J. Winfield and M. C. Berenbaum, *Biochem. J.*, 1989, **261**, 277–280.
57 B. A. Wagner, S. Venkataraman and G. R. Buettner, *Free Radical Biol. Med.*, 2011, **51**, 700–712.
58 L. Jamalzadeh, H. Ghafoori, R. Sariri, H. Rabuti, J. Nasirzade, H. Hasani and M. R. Aghamaali, *Avicenna J. Med. Biochem.*, 2016, **4**, 10–33453.
59 Y. Ilieva, L. Dimitrova, M. M. Zaharieva, M. Kaleva, P. Alov, I. Tsakovska, T. Pencheva, I. Pencheva-El Tibi, H. Najdenski and I. Pajeva, *Toxics*, 2021, **9**, 92.
60 M.-Y. Kang, I. Katz and B. Sapoval, *Respir. Physiol. Neurobiol.*, 2015, **205**, 109–119.
61 B. J. Matkowsky and Z. Schuss, *SIAM J. Appl. Math.*, 1982, **42**, 822–834.